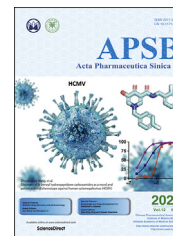Chinese Pharmaceutical Association
Institute of Materia Medica, Chinese Academy of Medical Sciences

Acta Pharmaceutica Sinica B

ORIGINAL ARTICLE

Targeting tumor endothelial hyperglycolysis enhances immunotherapy through remodeling tumor microenvironment

Yunlong Shan[a,†], Qi Ni[a,†], Qixiang Zhang[a,†], Mengying Zhang[a], Bin Wei[b], Lingge Cheng[a], Chongjin Zhong[a], Xinyu Wang[a], Qingqing Wang[a], Jiali Liu[a], Jingwei Zhang[a], Jingjing Wu[b,*], Guangji Wang[a,*], Fang Zhou[a,*]

[a]Key Laboratory of Drug Metabolism and Pharmacokinetics, State Key Laboratory of Natural Medicines, China Pharmaceutical University, Nanjing 210009, China
[b]Department of Hematology and Oncology, the Affiliated Huaian No. 1 People's Hospital of Nanjing Medical University, Huai'an 223300, China

Abstract Vascular abnormality is a hallmark of most solid tumors and facilitates immune evasion. Targeting the abnormal metabolism of tumor endothelial cells (TECs) may provide an opportunity to improve the outcome of immunotherapy. Here, in comparison to vascular endothelial cells from adjacent peritumoral tissues in patients with colorectal cancer (CRC), TECs presented enhanced glycolysis with higher glyceraldehyde-3-phosphate dehydrogenase (GAPDH) expression. Then an unbiased screening identified that osimertinib could modify the GAPDH and thus inhibit its activity in TECs. Low-dose osimertinib treatment caused tumor regression with vascular normalization and increased infiltration of immune effector cells in tumor, which was due to the reduced secretion of lactate from TECs by osimertinib through the inhibition of GAPDH. Moreover, osimertinib and anti-PD-1 blockade synergistically retarded tumor growth. This study provides a potential strategy to enhance immunotherapy by targeting the abnormal metabolism of TECs.

*Corresponding authors. Tel.: +86 25 83271176; fax: +86 25 83271060.
E-mail addresses: zf1113@163.com (Fang Zhou), guangjiwang@hotmail.com (Guangji Wang), wjj891208@163.com (Jingjing Wu).
†These authors contributed equally to this work.

1. Introduction

Colorectal cancer (CRC) has high metabolic requirements and uses multiple mechanisms to ensure sustained angiogenesis[1]. Tumor vasculature is a chaotic labyrinth of malformed and unstable blood vessels that is structurally and functionally abnormal[2−4]. Upon vascularization, tumor blood vessels supply tumors with constant oxygen and nutrients to support their continued growth and spread. Due to their critical roles in promoting tumor growth and metastasis, tumor blood vessels have become a major target for current anti-cancer therapy[5]. However, CRC patients with anti-angiogenesis therapy alone have no significant improvements in outcomes[6]. According to our previous studies, remodeling the homeostasis of tumor vasculature may enhance cancer chemotherapy[7,8]. Furthermore, a growing body of evidence has demonstrated that regulation of angiogenesis in tumor microenvironment can improve immuno-therapy and radiotherapy besides chemotherapy[9−11]. Vascular abnormality is a hallmark of most solid tumors and facilitates immune evasion. Compelling preclinical and clinical evidence reveals that anti-VEGF therapy creates a window of tumor vessel normalization with increased recruitment and anticancer activity of immune cells in the tumor microenvironment[12].

Recent studies have not only highlighted the importance of endothelial cell (EC) metabolism in angiogenesis[13,14], but also identified the specific metabolic profiles in ECs, which act as gatekeepers of immune cell infiltration into tumor tissues[15,16]. Under the circumstance of metabolic stress including hypoxia and acidosis that promote ECs proliferation and angiogenesis, tumor endothelial cells (TECs) upregulate the expression of a list of mediators in the metabolic pathway[3]. Moreover, the activated ECs tend to switch the metabolic phenotype[17] in need of development of a neovascular supply induced by angiogenic signals[18]. ECs then generate the majority of their energy relying on glucose, gluta-mine and fatty acids for migration and proliferation during angiogenesis, even though their proximity to blood oxygen[15,19]. Interestingly, recent studies have observed that enhanced glycol-ysis in ECs is accompanied by inflammatory response[20,21]. Tar-geting EC metabolism for the inhibition of pathological angiogenesis has received increasing attention. However, it is unknown whether targeting the metabolism of TECs could improve the efficacy of immune-checkpoint inhibitors.

Here, to unveil the role of endothelial metabolism in CRC pro-gression, we investigated the metabolic characteristics and GAPDH expression pattern of ECs in malignant tumors versus peritumoral tissues in humans and mice. On the basis of these results, we further screened two libraries on GAPDH function and identified osimerti-nib, an oral selective inhibitor of both epidermal growth factor re-ceptor (EGFR)-TKI (tyrosine kinase inhibitor)-sensitizing and EGFR T790M lung cancer, which might reduce the intensity of glycolysis of TECs by alkylating residue Cys247 of GAPDH. Our preclinical and clinical findings implied that low dose of osimertinib could remodel immunometabolic microenvironment by reducing the secretion of endothelial lactate, and thereby amplify the efficacy of PD-1 antibody for CRC immunotherapy.

2. Materials and methods

2.1. Human samples

Human colon tumor tissues and peritumoral tissues were obtained from the Affiliated Huaian No. 1 People's Hospital of Nanjing Medical University. This study was approved by the Human Ethics Committee of the Affiliated Huaian No. 1 People's Hospital of Nanjing Medical University (ID: YX-2021-021-01). Written informed consent was obtained from the patients.

2.2. Materials and reagents

Osimertinib (AZD9291) and almonertinib (HS-10296) were kindly provided by Hansoh Pharma Co., Ltd. (Jiangsu, China). All drugs were dissolved in dimethyl sulfoxide (DMSO) to create stocks at a concentration of 40 mmol/L and stored in aliquots at −80 °C. The drugs were warmed with 50 °C water bath for 30 min before use. All therapeutic monoclonal antibodies (mAbs) were purchased from BioXCell. Control IgG was rat IgG2α (BE0089, BioXCell, New Hampshire, USA). For CD8$^+$ T cell or macro-phage depletion, 1 mg of anti-CSF1 antibody (BE0204) or anti-CD8 antibody (BE0117) were intraperitoneally injected 2 days before treatment initiation and then with 0.5 mg twice a week for 2 weeks study. Therapeutic mAb used in the study was rat anti-PD-1 antibody (BP0146, 5 mg/kg). Therapeutic and control IgG were administered twice a week. Treatment of C57Bl6/J mice carrying subcutaneous MC38 tumors was started when the tumors became palpable and had a mean volume of 50−100 mm^3.

2.3. Animal experiment

Female C57BL/6 mice and BALB/c mice (6−8 weeks old, 18−22 g) were purchased from the Model Animal Genetics Research Center of Nanjing University (Nanjing, China). Tumor model was established by injection of 1×10^6 cancer cells sub-cutaneously into the right flank of mice. The tumors were grown for several weeks, either according to a "survival" schedule (endpoint defined by tumor volume) or a fixed time-point (endpoint defined as fixed time lapsed after tumor challenge). Tumor size was determined by caliper measurements and calcu-lated according to Eq. (1):

$$V = 0.5 \times \left(L \times S^2\right) \tag{1}$$

where S is the short, and L is the long tumor axis.

Tumor weight measurements were performed post-mortem. All efforts were made to minimize the animals' suffering and to reduce the number of animals used. All animal care and experi-mental procedures were conducted according to the National Research Council's Guidelines for the Care and Use of Laboratory Animals and were approved by Animal Ethics Committee of China Pharmaceutical University (Animal Authorization Refer-ence Number: SYXK2016-0011).

2.4. Metabolomic profile assessment

For metabolites extraction, 2×10^6 cells were washed three times with cold phosphate buffered saline (PBS) and pelleted by centri-fugation. Cell pellets were then flash frozen in liquid nitrogen and stored at −80 °C until further processing. After the addition of 200 μL of extract solution (acetonitrile:methanol = 1:1, containing isotopically-labelled internal standard mixture), the samples were vortexed for 30 s, sonicated for 10 min in ice-water bath, and incubated for 1 h at −40 °C to precipitate proteins. Then the samples were centrifuged at 10,000×g for 15 min at 4 °C. The resulting supernatant was transferred to a fresh glass vial for anal-ysis. The quality control (QC) sample was prepared by mixing an equal aliquot of the supernatants from all of the samples. These

samples were then analyzed by tandem mass spectrometry coupled with liquid chromatography (LC−MS/MS).

LC−MS/MS analyses were performed using an ultra-high performance liquid chromatography (UHPLC) system (Thermo Fisher Scientific, Waltham, MA, USA) with a UPLC BEH Amide column (2.1 mm × 100 mm, 1.7 μm) coupled to Q Exactive HFX mass spectrometer (Orbitrap MS, Thermo Fisher Scientific). The mobile phase consisted of 25 mmol/L ammonium acetate and 25 ammonia hydroxide in water (pH 9.75) (A) and acetonitrile (B). The auto-sampler temperature was set at 4 °C and the injection volume was 3 μL.

The QExactive HFX mass spectrometer was used for its ability to acquire MS/MS spectra in information-dependent acquisition (IDA) mode in the control of the acquisition software (Xcalibur, Thermo Fisher Scientific). The parameters were set as following: sheath gas flow rate as 30 Arb, Aux gas flow rate as 25 Arb, capillary temperature 350 °C, full MS resolution as 60,000, MS/MS resolution as 7500, collision energy as 10/30/60 in NCE mode, spray voltage as 3.6 kV (positive) or −3.2 kV (negative), respectively.

The raw data generated from the MS were converted to the mzXML format using ProteoWizard and processed with an in-house program, which was developed using R and based on XCMS, for peak detection, extraction, alignment, and integration. Then an in-house MS2 database (BiotreeDB) was applied in metabolite annotation. The cutoff for annotation was set at 0.3.

2.5. Drug affinity-responsive target stabilization assay

Approximately 10^6−10^7 cells were lysed with NP-40 (Beyotime, Shanghai, China) at 4 °C for 30 min and protein concentration of the lysate was measured by the BCA protein assay kit (Thermo Fisher Scientific). Osimertinib dissolved in 1 × TNC buffer (50 mmol/L Tris, 50 mmol/L NaCl, 10 mmol/L CaCl₂, pH 7.4) was added into the cell lysate to reach the indicated concentrations and gently mixed. The lysates were then placed at room temperature for 2 h to allow sufficient ligand−protein target interactions, and then digested by Pronase (Roche, Basel, Switzerland, dissolved in 1 × TNC buffer) at indicated concentrations for precisely 30 min at room temperature. Proteolysis was quenched by mixing the lysate with 4 × loading buffer (Bio-Rad, Hercules, CA, USA) and 5 min of boiling.

2.6. LC−MS/MS protein data processing and analysis

Recombinant GAPDH (10 μg) was diluted to 500 μL in PBS treated with 200 μmol/L osimertinib for 2 h at room temperature and stopped by 4 × loading buffer (Bio-Rad) and 5 min of boiling. The samples were separated by SDS-PAGE, then stained by Coomassie brilliant blue (CBB).

The tryptic digested peptides were obtained as the protocol described previously[22]. The gel bands were cut into pieces and washed with Milli-Q water, then, CBB dye was removed with 50% acetonitrile (ACN)/50 mmol/L ammonium bicarbonate. The gel slices were dehydrated twice in 100% ACN for 30 min and reconstituted in 50 mmol/L ammonium bicarbonate containing 10 ng/μL sequencing-grade trypsin (Promega, Madison, WI, USA) to digest proteins at 37 °C for 16 h. The tryptic digested peptides were extracted from the gel pieces with 50% ACN/0.1% TFA and lyophilized by vacuum centrifugation.

The identification of the peptides of GAPDH was performed on an EASY-nLC 1000 system coupled to an Orbitrap Fusion mass spectrometer (Thermo Fisher Scientific) equipped with an online nano-electrospray ion source. The peptides were resuspended with 10 μL solvent A (0.1% formic acid in water), and 8 μL peptide sample was loaded onto the trap column (Acclaim PepMap C18, 100 μm × 2 cm, Thermo Fisher Scientific) with a flow rate of 10 μL/min for 3 min and subsequently separated on the analytical column (Acclaim PepMap C18, 75 μm × 25 cm) with a linear gradient. The gradient started from 2% phase B (90% acetonitrile, 0.1% formic acid in water) to 35% phase B in 75 min, 35%−60% phase B in 5 min, 60%−90% phase B in 5 min, and 90%−2% phase B in 5 min. The column flow rate was maintained at 300 nL/min.

The Orbitrap Fusion mass spectrometer was operated in the data-dependent acquisition mode to switch automatically between MS and MS/MS acquisition. Survey full-scan MS spectra (m/z 350−1600) were acquired in Orbitrap with a mass resolution of 60,000, the AGC target was set to 1×10^6, and the maximum injection time was 50 ms. MS/MS acquisition was performed in top speed mode with 3 s cycle time in orbitrap, the mass resolution was set to 15,000, the maximum injection time was 80 ms, the AGC target was set to 1×10^5, and the isolation window was set at m/z 1.6. Ions with charge states +2, +3 and + 4 were sequentially fragmented by higher energy collisional dissociation (HCD) with a normalized collision energy (NCE) of 30%. In all cases, one microscan was recorded using dynamic exclusion of 30 s. MS/MS fixed first mass was set at 110. The spectra were recorded with Xcalibur (version 3.0.63.3) software.

The raw mass files generated by the LC−MS/MS were then processed using pFind (3.1.5) software[23] for the identification of the modified peptides on GAPDH protein. Data were searched against the human HSPA8 protein (Uniport ID: P04406) fasta sequence. The parameters for database search were set as follows: (1) enzyme: Trypsin KR_C; (2) max missing cleavage number: 2; (3) MS and MS/MS tolerance: 20 ppm and 0.2 Da; (4) variable modifications: oxidation on M residue, osimertinib ($C_{28}H_{33}N_7O_2$, 499.269573 Da) on residue C; (6) the result filter was set as: the false discovery rate (FDR) ≤ 1% at peptide level, minimum peptide length ≥ 6. The MS/MS spectra were extracted by pBuild (3.1.0), the compatible software in pFind suite.

2.7. Osimertinib distribution in mouse CRC model

Osimertinib (25 mg/kg) was administered orally to female BALB/c mice bearing CT26 tumor xenografts with animals terminated (rising CO₂ dose) and blood and tumor samples collected at 4 h postdose. Tumors tissues were dissociated using a mouse tumor dissociation kit (130-096-730, Miltenyi Biotec, Bergisch Gladbach, Germany). The digested cells were filtered with a 40 μm nylon mesh to remove cell clumps and washed in washing buffer (PBS containing 5 mmol/L EDTA and 2% FBS). All single-cell suspensions were purified by CD31 MicroBead (130-097-418, Miltenyi Biotec), the other cells were non-endothelial cells.

Osimertinib in serum, tumors tissues or cells were extracted in acetonitrile, containing internal standard (almonertinib), and then can be quantitatively analyzed by a ultra-performance LC system (Shimadzu, Japan) coupled to an API 4000 triple quadrupole mass spectrometer (Applied Biosystems) outfitted with a turbo ionspray ionization source. The chromatographic separation was achieved on a Luna® column (Phenomenex, C18(2) 100 Å, LC 250 mm × 4.6 mm, 5 μm). The binary solvent system was composed of 5 mmol/L ammonium acetate and 0.1% in H₂O (phase A) and methanol (phase B). The gradient of the binary

solvent used a gradient as follows: 1% phase B maintained for 1 min, increased to 70% at 5 min and held for 3 min, and then decreased to 1% at 9.5 min followed by 2.5 min for equilibration at a rate of 0.2 mL/min. The following transitions were detected: m/z 526.5 → m/z 451.3 (osimertinib), m/z 500 → m/z 455.5 (IS). Data were processed by Analyst 1.5.2 (Applied Biosystems, Waltham, MA, USA). Experiments were performed with biological replicates ($n = 5$).

2.8.   Determination of thiol reactivity

As the thiol donor, cysteamine (Sigma−Aldrich, Burlington, MA, USA) aqueous (10 mmol/L) was diluted with 100 mmol/L phosphate buffer (pH 7.4) to make 1 × cysteamine solution (0.5 mmol/L). The stock solution of test compounds was diluted with 100 mmol/L phosphate buffer (pH 7.4) to a given concentration. For preparation of DTNB regent, 0.014 mmol DTNB (Sigma−Aldrich) and 0.5 mmol sodium hydrogen carbonate was dissolved in 25 mL of 100 mmol/L phosphate buffer (pH 7.4). Cysteamine solution (0.5 mmol/L) was mixed with an equal volume of test compound solution, and quickly transferred into a 96-well plate. At different time points, reduced thiol groups were quantified with DTNB. One minute after DTNB was added, the absorption was measured at $\lambda = 405$ nm using a Synergy H1 microplate reader (BioTek, Winooski, Vermont, USA). The quantification of the remaining cysteamine was carried out by the calibration curve of thiol content $vs.$ absorbance.

2.9.   Statistical analysis

Error bars indicate the standard error of the mean (SEM). The number of biological (nontechnical) replicates for each experiment is indicated in the figure legends. Independent experiments are presented individually or combined, as explained in the figure legends. Analysis of experiments with more than two groups was performed using one-way ANOVA with Tukey's correction for multiple comparisons, unless indicated otherwise. For experiments with two groups, statistical analysis was performed using Student's t-test with 95% confidence interval. Statistical analyses in the survival experiments were performed by log-rank (MantelCox) test. Statistical significance is indicated in the figures.

3.   Results

3.1.   The expression of tumor endothelial GAPDH is enhanced in CRC patients and mouse model

To examine the metabolic profile of CD31$^+$ ECs in tumor tissues and adjacent peritumoral tissues, we isolated human tumor endothelial cells (hTECs) and paired adjacent endothelial cells (hAECs) from 4 CRC patients and detected the purity of CD45$^-$CD31$^+$ ECs by flow cytometry (Supporting Information Fig. S1A). Liquid chromatography−tandem mass spectrometry (LC−MS/MS) based metabolomics analysis was used to differentiate metabolic differences between hAECs and hTECs (Fig. 1A). Metabolic pathway analysis revealed that the relative intracellular metabolite levels of glycolysis, pentose phosphate pathway (PPP) and aminoacyl-tRNA biosynthesis pathway were changed in hTECs relative to their paired hAECs (Fig. 1B). Notably, unlike the intermediates of PPP and aminoacyl-tRNA biosynthesis pathways, most of the glycolytic intermediates were significantly altered in hTECs (Fig. S1B−S1D). Measurements of the extracellular

acidification rate (ECAR) revealed significant enhancement of aerobic glycolysis and glycolytic capacity in hTECs compared with hAECs (Fig. 1C and D). Surprisingly, compared with hAECs, the glycolysis increased by 43.23% in hTECs (Fig. 1D). Given that GAPDH is the key glycolytic enzyme for immunoregulation[24,25], we next investigated whether the protein level of GAPDH was related to the different levels of aerobic glycolysis between hTECs and hAECs. Endothelial GAPDH levels in human CRC tissues were significantly higher than those in adjacent peritumoral tissues by both flow cytometry (Fig. 1E and Fig. S1E) and immunoblotting (Fig. 1F).

The isolated CD45$^-$CD31$^+$ ECs from tumors and lungs in xenograft mice were then investigated. As shown in Fig. 1G and H, the glycolysis level in mouse tumor endothelial cells (mTECs) was much higher than that in normal endothelial cells (mNECs). Likewise, flow cytometry revealed that GAPDH expression in mTECs was higher than that in mNECs (Fig. 1I, Fig. S1F and S1G). Additionally, immunoblot assay demonstrated that robust GAPDH expression in mTECs was visualized compared with mNECs (Fig. 1J and Fig. S1H). According to these results, we concluded that the glycolytic enzyme GAPDH and glycolysis are increased in the TECs of CRC.

3.2.   Osimertinib inactivates GAPDH via covalent modification of cysteine residues

GAPDH activity assays in human umbilical venous endothelial cells (HUVECs) and recombinant GAPDH were performed to identify potential GAPDH inhibitors among all of U.S. Food and Drug Administration (FDA)-approved kinase inhibitors (62 compounds) and an in-house collection of FDA-approved non-kinase inhibitor (27 compounds) in clinic. Of note, both screens yielded an overlapping set of FDA-approved inhibitors in light of top five candidates that were able to reduce GAPDH activity, an oral EGFR-TKI osimertinib (Fig. 2A and B). Osimertinib also exhibited a dose-dependent inhibitory effect on the catalytic activity of GAPDH in HUVECs (Fig. 2C). Consistently, the recombinant GAPDH activity in cell-free system and the lactate level in HUVECs were reduced by osimertinib (Supporting Information Fig. S2A and S2B).

Next, drug affinity responsive target stability (DARTS) assay[26] was performed to investigate whether GAPDH inhibition by osimertinib can be attributed to the direct binding interaction. As expected, GAPDH was conserved after a series of pronase ratios to cell lysate with or without osimertinib treatment (Fig. 2D), indicating that GAPDH is a potential target of osimertinib. Since osimertinib is a covalent small-molecule inhibitor that modifies EGFR at site of T790M mutation[27], the modification of osimertinib on GAPDH was further explored by LC−MS/MS. The results revealed that the mass of GAPDH peptide (amino acid residues 235−248) involving site Cys247 increased by 499.27 Da following osimertinib treatment, which is consistent with alkylation by osimertinib (Fig. 2E). In other words, Cys247 of GAPDH can be modified by osimertinib (Fig. 2F and Fig. S2C). In contrast, the modification was not observed at any cysteine in DMSO-treated GAPDH (Fig. 2E). Additionally, determination of thiol reactivity revealed that osimertinib reduced the concentration of free cysteamine in a dose- and time dependent manner (Fig. S2D and S2E).
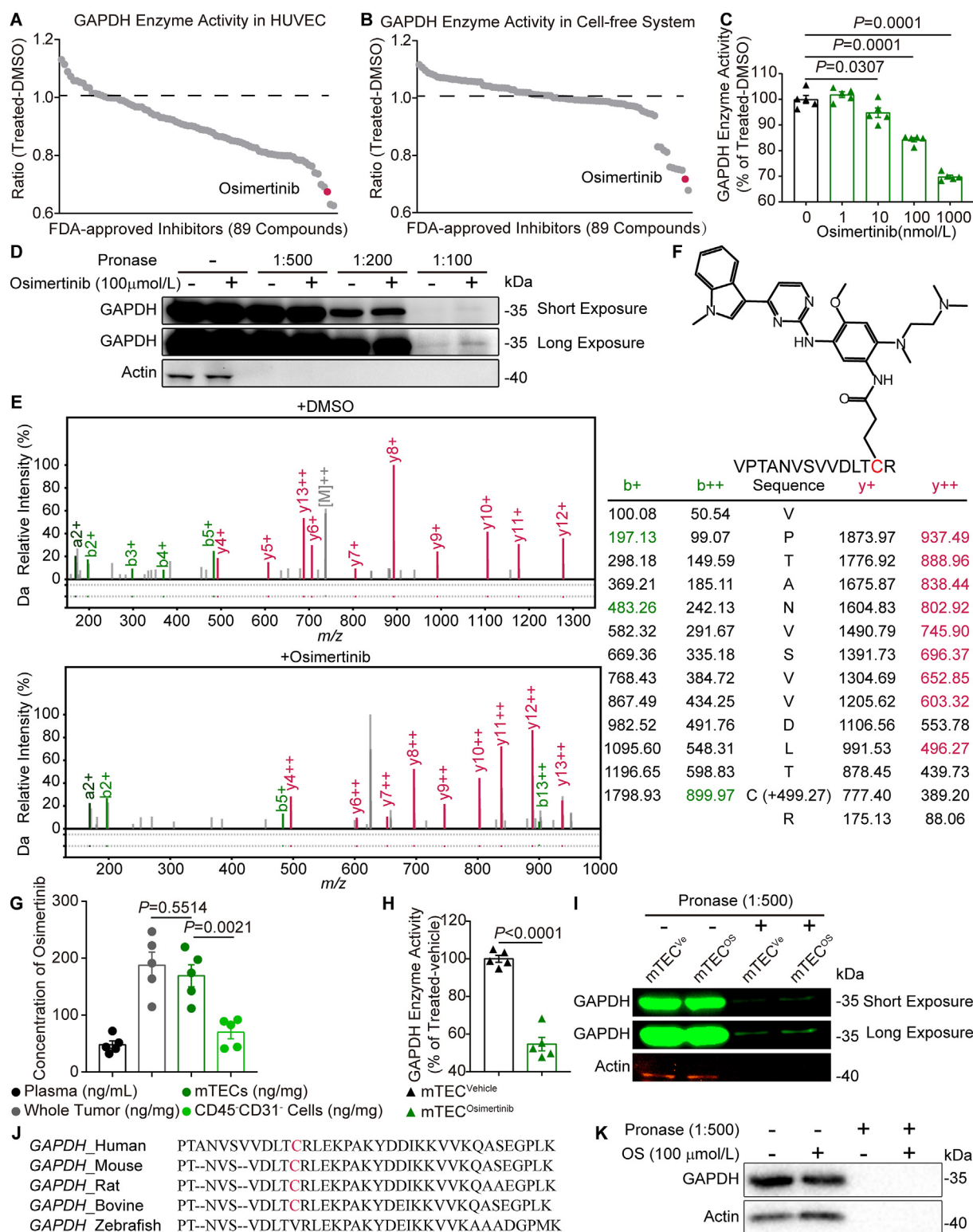
There was a high accumulation of osimertinib in tumors from xenograft mice compared to the plasma samples. In particular, the concentration in the isolated mTECs was significantly higher than
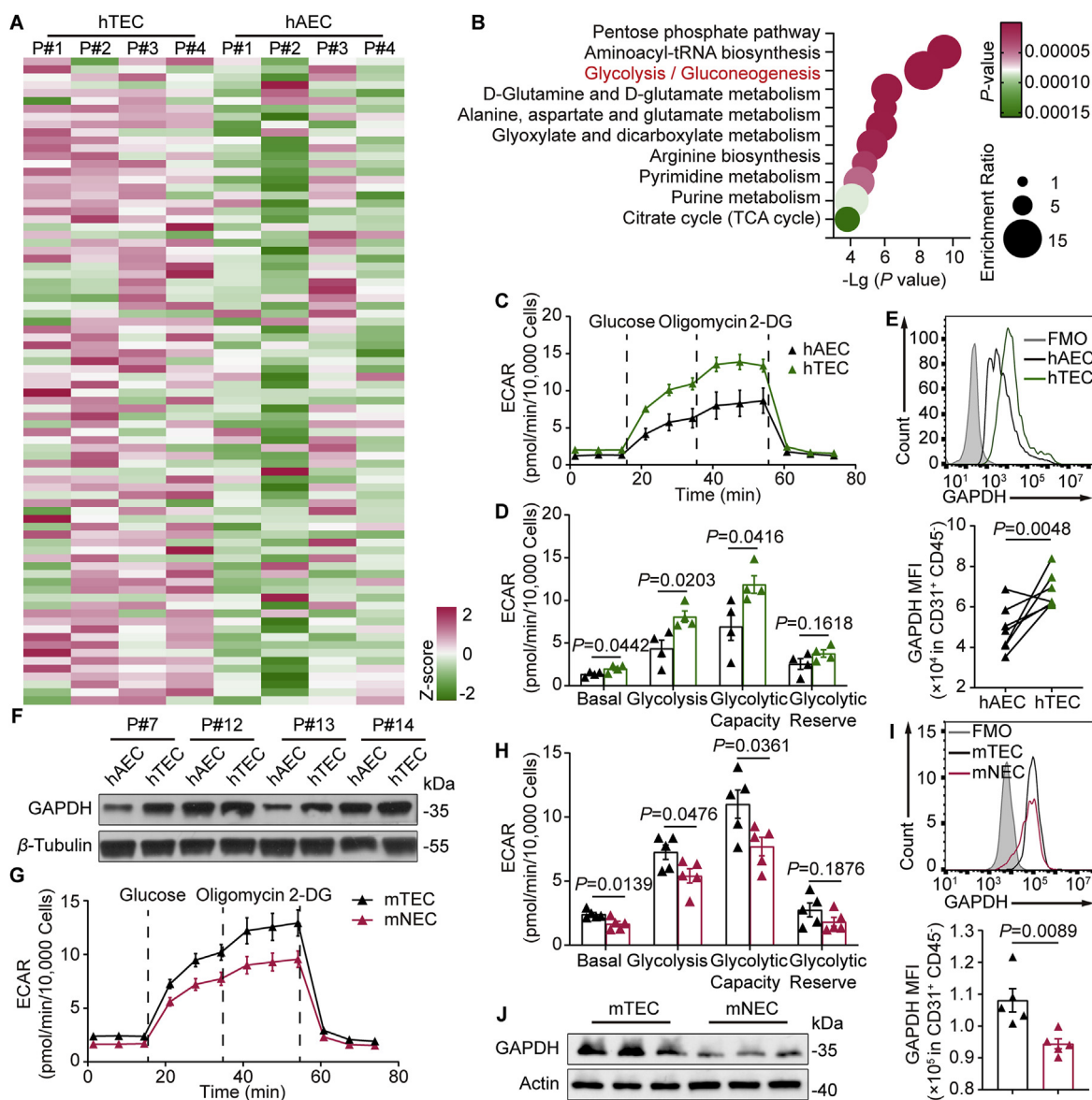
Figure 1 The expression of tumor endothelial GAPDH is enhanced in CRC patients and mouse model. (A) Correlation heatmap and (B) enrichment analysis of metabolites in CD31$^+$ endothelial cells of tumors *versus* matched adjacent peritumoral tissues from 4 CRC patients. (C) Representative trace of extracellular acidification rate (ECAR) values from a glycolysis stress test using XF-96 analyzer showing CD31$^+$ endothelial cells of CRC patients' tumors *versus* matched adjacent peritumoral tissues. $n = 4$. (D) Quantification of sequential compound injections measuring glycolysis, glycolytic capacity, glycolytic reserve and non-glycolytic acidification. $n = 4$. (E) Top, flow cytometry analysis of GAPDH expression in CD45$^-$CD31$^+$ endothelial cells. Bottom, GAPDH levels in CD45$^-$CD31$^+$ endothelial cells were compared between tumors and paired adjacent peritumoral tissues from 7 patients with CRC. (F) The protein level of GAPDH of CD31$^+$ endothelial cells in tumors and para-carcinoma tissues from CRC patients was detected by immunoblot. (G) Comparison of ECAR from CD31$^+$ endothelial cells in mouse transplanted CT26 tumors *versus* lungs. $n = 5$. (H) Quantification of glycolysis, glycolytic capacity, glycolytic reserve and non-glycolytic acidification as shown in G. $n = 5$. (I) The mean of GAPDH fluorescence intensity analyzed by flow cytometry from CD31$^+$ endothelial cells in the indicated groups. $n = 5$. (J) Immunoblot analysis of GAPDH in CD31$^+$ endothelial cells from mouse tissues as shown in G. Statistical analysis by unpaired Student's *t*-test. Data are presented as mean ± SEM. hTEC, human tumor endothelial cells; hAEC, paired adjacent human endothelial cells; mTEC, mouse tumor endothelial cells; mNEC, normal mouse endothelial cells.

that in the CD45$^-$CD31$^-$ cells (169 ± 38 *vs*. 70 ± 22 ng/mg protein) (Fig. 2G) without obvious toxicity[28]. In isolated mTECs from osimertinib-treated group, GAPDH activity was remarkably lower than that from vehicle group (Fig. 2H), but not in isolated CD45$^-$CD31$^-$ cells after the separation and removal of CD45$^+$ leukocytes and CD31$^+$ endothelial cells (Fig. S2F). Consistent with

the DARTS in HUVECs, GAPDH became less susceptible to pronase digestion in the isolated mTECs from CT26 tumor-bearing mice (Fig. 2I). GAPDH protein contains a conserved region in various species, whereas cysteine 245 is replaced by valine in GAPDH of zebrafish (Fig. 2J). To further investigate whether the covalent modification of GAPDH by osimertinib was based on

The peptide sequence table (from panel E/F):

b+	b++	Sequence	y+	y++
100.08	50.54	V		
197.13	99.07	P	1873.97	937.49
298.18	149.59	T	1776.92	888.96
369.21	185.11	A	1675.87	838.44
483.26	242.13	N	1604.83	802.92
582.32	291.67	V	1490.79	745.90
669.36	335.18	S	1391.73	696.37
768.43	384.72	V	1304.69	652.85
867.49	434.25	V	1205.62	603.32
982.52	491.76	D	1106.56	553.78
1095.60	548.31	L	991.53	496.27
1196.65	598.83	T	878.45	439.73
1798.93	899.97	C (+499.27)	777.40	389.20
		R	175.13	88.06

Figure 2 Osimertinib inactivates GAPDH *via* covalent modification of cysteine residues. (A) HUVECs were treated with the compounds from the FDA-approved inhibitors at a concentration of 1 μmol/L for 12 h, followed by the assessment of GAPDH enzyme activity. Dots in gray represent inhibitors. Osimertinib is indicated in fuchsine. Data represent the mean of three independent experiments. $n = 3$. (B) Recombinant GAPDH was treated with the FDA-approved inhibitors (final concentration 100 μmol/L) or DMSO for 2 h, followed by enzyme activity assay. Data represent the mean of three independent experiments. $n = 3$. (C) Dose-dependent inactivation of GAPDH enzyme activity in HUVECs were treated with the indicated osimertinib concentrations for 12 h $n = 5$. (D) Immunoblot confirmed the stabilization of GAPDH by osimertinib (100 μmol/L) treatment for 2 h in HUVEC cell lysates in the DARTS assay. (E) Tandem mass spectrometry spectrum of the peptide in recombinant human GAPDH containing the osimertinib-adducted at residue Cys247. (F) Schematic diagram of GAPDH thiol group that was

selective binding to the site of Cys247, interactions of GAPDH with osimertinib was tested by DARTS in zebrafish embryos. The result of DARTS confirmed that GAPDH could not bind with osimertinib in zebrafish lysates (Fig. 2K), further demonstrating that Cys247 of GAPDH acted as the modification site by osimertinib.

3.3. GAPDH inactivation by osimertinib reduces aerobic glycolysis in TECs

To elucidate the effects of osimertinib on glycolysis in tumor vessels, mTECs were isolated from tumor bearing mice in the absence and presence of osimertinib. Continuous treatment with osimertinib (1 mg/kg, intragastrically) for 14 days led to lower ECAR in mTECs (Fig. 3A and Supporting Information Fig. S3A). A prominent reduction in glycolysis and glycolytic capacity was observed in mTEC^{osimertinib} compared with mTEC^{vehicle} (Fig. 3B and Fig. S3B). The lower ECAR was detected in MC38 cells and CT26 cells after osimertinib treatment (Fig. S3C and S3D), but 14-day treatment with osimertinib in mice subcutaneously transplanted MC38 cells had no effect on ECAR of the isolated tumor cells (Fig. S3E and S3F). Given that ECs tended to switch the metabolic phenotype for their energetic needs under stress[17], we also evaluated whether osimertinib would promote oxygen consumption rate (OCR). We found that OCR was not altered either in mTECs or in HUVECs treated with osimertinib (Fig. S3G−S3J). In addition, the mRNA level of gene signatures associated with oxidative phosphorylation (OXPHOS) in HUVECs treated with or without osimertinib exhibited no difference (Fig. S3K). HUVECs treated with osimertinib resulted in blockade in glycolytic flux at GAPDH, as evidenced by the increased level of dihydroxyacetone phosphate/glyceraldehyde 3-phosphate (the upstream metabolite of GAPDH) and the reduced level of 2-phosphoglyceric acid/3-phosphoglyceric acid (the downstream metabolite of GAPDH) (Fig. 3C and Fig. S3L). The level of lactate (the end-product of glycolysis) was further quantitatively detected. As shown in Fig. 3D, treatment with osimertinib decreased the generation of lactate in HUVECs. In contrast, GAPDH overexpression reversed the decreased lactate production and the impaired glycolytic flux induced by osimertinib (Fig. 3C and D). The rate of glycolysis was then measured using ECAR. The results showed that osimertinib treatment significantly attenuated ECAR compared with the control group (Fig. 3E and F). Consistently, osimertinib-induced ECAR inhibition was also reversed by GAPDH overexpression (Fig. 3E and F), indicating that GAPDH was required for the suppression of glycolysis by osimertinib in ECs.

3.4. Low dose of osimertinib leads to marked survival benefits and increased tumor necrosis in mouse CRC models

After verification of the inhibition of cell viability in MC38, CT26 and HUVEC cells by osimertinib (Supporting Information Fig. S4A), the functional roles of osimertinib were investigated in vivo. As shown in Fig. 4A, low-dose osimertinib (1 mg/kg, daily

for 14 days by oral gavage) markedly inhibited the tumor growth in MC38 tumor-bearing mice. Compared with vehicle group, the tumor volumes in osimertinib group were reduced by 55.88% at the end point of the study. Furthermore, the average weight of tumors from osimertinib group was significantly decreased (Fig. 4A). Osimertinib also extended the survival of the mice [Median (50%) survival: vehicle group, 22 days and osimertinib group, 27.5 days] (Fig. 4B). Similar effects of osimertinib on CT26 tumors were also observed in xenograft mice (Fig. 4C). These findings indicate that osimertinib gives rise to remarkable survival benefits in mouse models of colon cancer.

Immunohistochemistry confirmed that osimertinib treatment significantly decreased the proliferation of tumor cells in CRC mice, as reflected by the reduction in Ki67$^+$ cell percentage (Fig. 4D). Notably, while cell death labelled by cleaved caspase-3 (CC3) antibody was rarely observed in vehicle group, osimertinib significantly increased cell death (Fig. 4E). Because osimertinib did not affect cell viability of any colon cancer cells or ECs with plasma concentration (Fig. 2G and Fig. S4A), osimertinib-mediated cancer cell death did not account for direct effect. In addition, the blockade of the glycolytic flux in TECs treated with osimertinib was verified (Fig. S4B and S4C). Collectively, these data suggest that low dose osimertinib significantly increases overall survival through inducing regression of colon cancer.

3.5. Osimertinib ameliorates tumor angiogenesis and triggers antitumor-macrophages infiltration

To explore the effects of osimertinib on tumor vessels in vivo, flow cytometry and immunostaining were performed. Blood vascular density was significantly decreased in tumor tissues from osimertinib group (Fig. 5A and B). In line with this, flow cytometry analysis showed that osimertinib decreased the number of CD45$^-$CD31$^+$ vascular ECs from the tumors in mice (Fig. 5C). In analysis of structural changes of tumoral vessels, osimertinib group showed an increase in α-SMA$^+$ pericyte coverage around tumor vessels (Fig. 5A and D). In addition, immunofluorescence staining revealed that osimertinib markedly reduced GLUT1 (alternative hypoxia marker) expression (Supporting Information Fig. S5A). The reduction of tubulogenesis by osimertinib was diminished or almost completely reversed by overexpression of GAPDH in HUVECs (Fig. 5E and F). These results were also confirmed by the migration assay of HUVECs (Fig. S5B). However, osimertinib failed to inhibit the length (Fig. 5G and H) and number (Fig. 5I) of intersegmental vessels (ISVs) in zebrafish embryos, which may be due to the different amino acid sequence of GAPDH (C245V) in ECs of zebrafish. These results indicate that low-dose osimertinib strikingly suppresses angiogenesis with increased pericyte coverage of the remaining blood vessels via alkylation of GAPDH at residue Cys245.

The suppression of angiogenesis along with the increased pericyte coverage of tumor blood vessels is now considered as a phenomenon of the improved vascular function in tumor, a

---

covalently modified by osimertinib. (G) Concentration of osimertinib in mouse plasma, whole tumor tissues, CD31$^+$ tumor endothelial cells and CD31$^-$ non-endothelial cells at 4 h after osimertinib treatment (25 mg/kg) by oral gavage. $n = 5$. (H) Mice were treated with osimertinib (25 mg/kg) by oral gavage; after 4 h, the mice were sacrificed and lysates of CD45$^-$CD31$^+$ endothelial cells from mouse transplanted CT26 tumors were used for GAPDH enzyme activity assay. $n = 5$. (I) Immunoblot confirmed the stabilization of GAPDH by osimertinib (25 mg/kg) or vehicle for 4 h in CD31$^+$ endothelial cell lysates from mouse transplanted CT26 tumors in the DARTS assay. (J) Alignment of the GAPDH motif in the indicated species. (K) DARTS confirmed that GAPDH could not bind with osimertinib in zebrafish embryos lysates after osimertinib (100 μmol/L) treatment for 2 h. Statistical analysis by unpaired Student's t-test or one-way ANOVA. Data are presented as mean ± SEM.
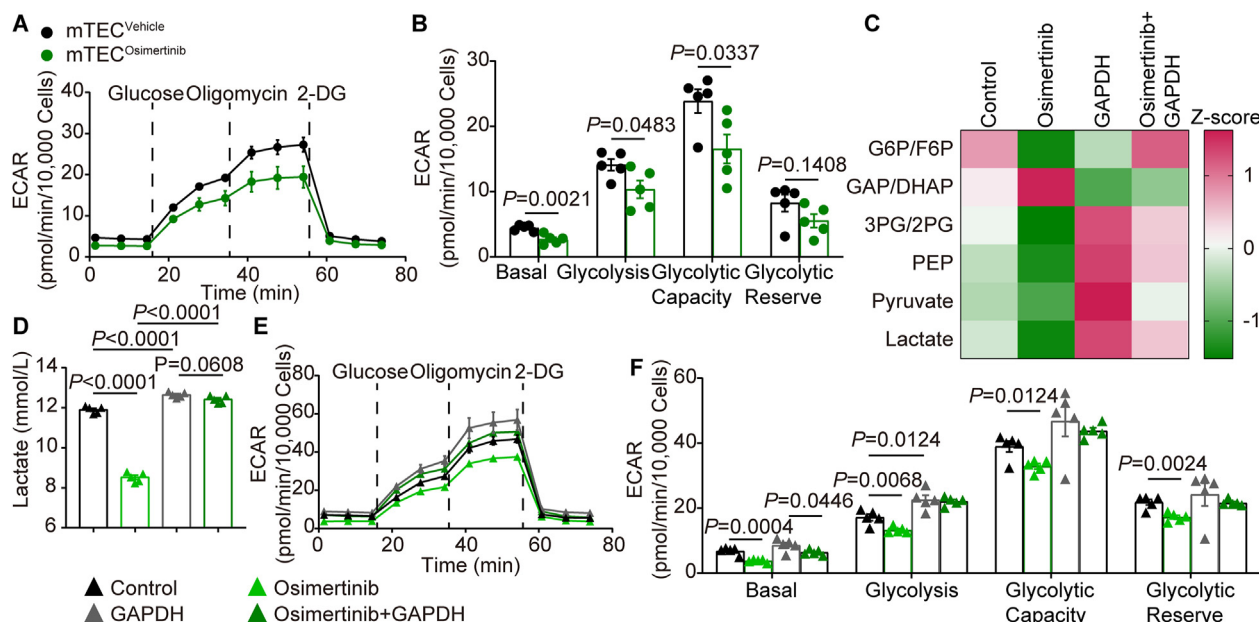
Figure 3 GAPDH inactivation by osimertinib reduces aerobic glycolysis in TECs. (A) Comparison of ECAR in CD45$^-$CD31$^+$ endothelial cells from transplanted CT26 tumors after treatment of mice with osimertinib (1 mg/kg) or vehicle daily for 14 days by oral gavage. (B) Quantification of sequential compound injections measuring glycolysis, glycolytic capacity, glycolytic reserve and non-glycolytic acidification as shown in (A). (C) HUVECs were treated with osimertinib or DMSO for 24 h after overexpression with GAPDH vector for 24 h. Glycolytic intermediates were measured from lysates *via* LC−MS/MS. Heat map showed the blockade of the glycolytic flux at the level of GAPDH. (D) Lactate levels of HUVECs treated as indicated in (C). (E) Glycolysis was measured *via* Seahorse extracellular flux analyzer in HUVEC as indicated treatment. (F) Quantification of glycolysis, glycolytic capacity, glycolytic reserve and non-glycolytic acidification as shown in (E). Statistical analysis by unpaired Student's *t*-test or one-way ANOVA. Data are presented as mean ± SEM (*n* = 5). G6P, glucose-6-phosphate; F6P, fructose-6-phosphate; GAP, glyceraldehyde-3-phosphate; DHAP, dihydroxyacetone phosphate; 3PG, 3-phosphoglycerate; 2PG, 2-phosphoglycerate and PEP, phosphoenolpyruvate.
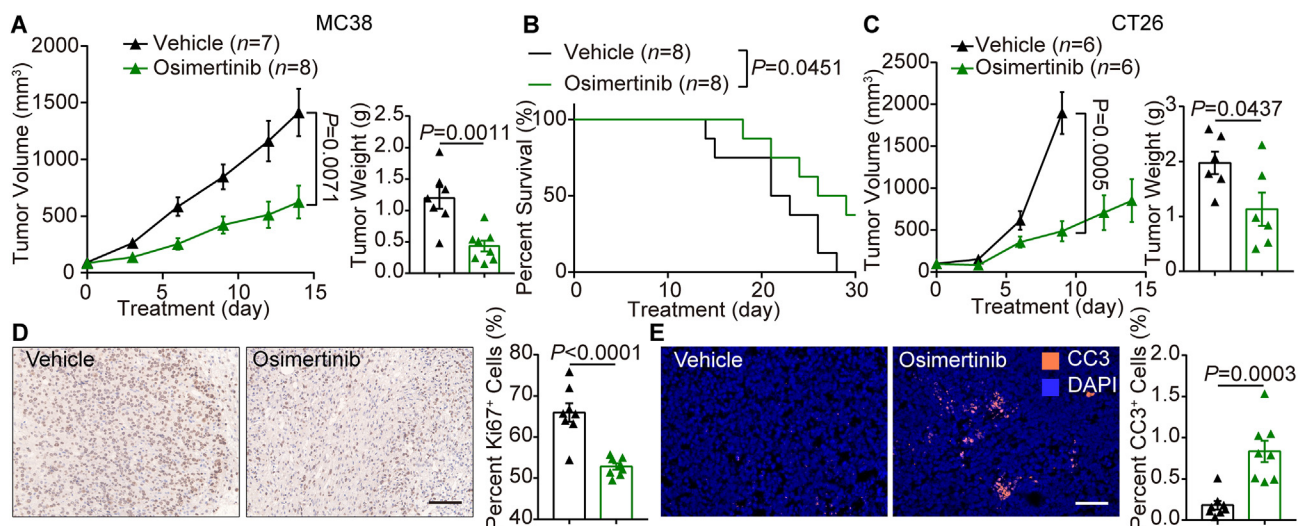
Figure 4 Low dose of osimertinib leads to marked survival benefits and increased tumor necrosis in mouse CRC models. (A) Left, volume of subcutaneous MC38 tumors treated with vehicle or osimertinib (1 mg/kg) daily for 14 days by oral gavage. Right, tumor weight at necropsy. (B) Kaplan−Meier survival curves of two indicated groups. (C) Left, volume of subcutaneous CT26 tumors in two indicated groups treated as (A). Right, tumor weight at necropsy. Statistical analysis by unpaired Student's *t*-test. (D) Left, representative images of Ki67 immunostaining and nuclear staining of MC38 tumors in two indicated groups. Right, quantitative analysis of the relative nuclear Ki67 in vehicle group and osimertinib group. Each dot indicates one tumor and represents the average of 5 images. *n* = 8. (E) Left, representative images of cleaved caspase-3 (CC3) staining (orange) and 4′,6-diamidino-2-phenylindole (DAPI) nuclear staining (blue) of MC38 tumors in two indicated groups. Right, quantitative analysis of the relative cell death in vehicle group and osimertinib group. Each dot indicates one tumor per mouse and represents the average of 5 images. *n* = 8. Statistical analysis by unpaired Student's *t*-test or log-rank test. Data are mean ± SEM. Scale bar = 100 μm.
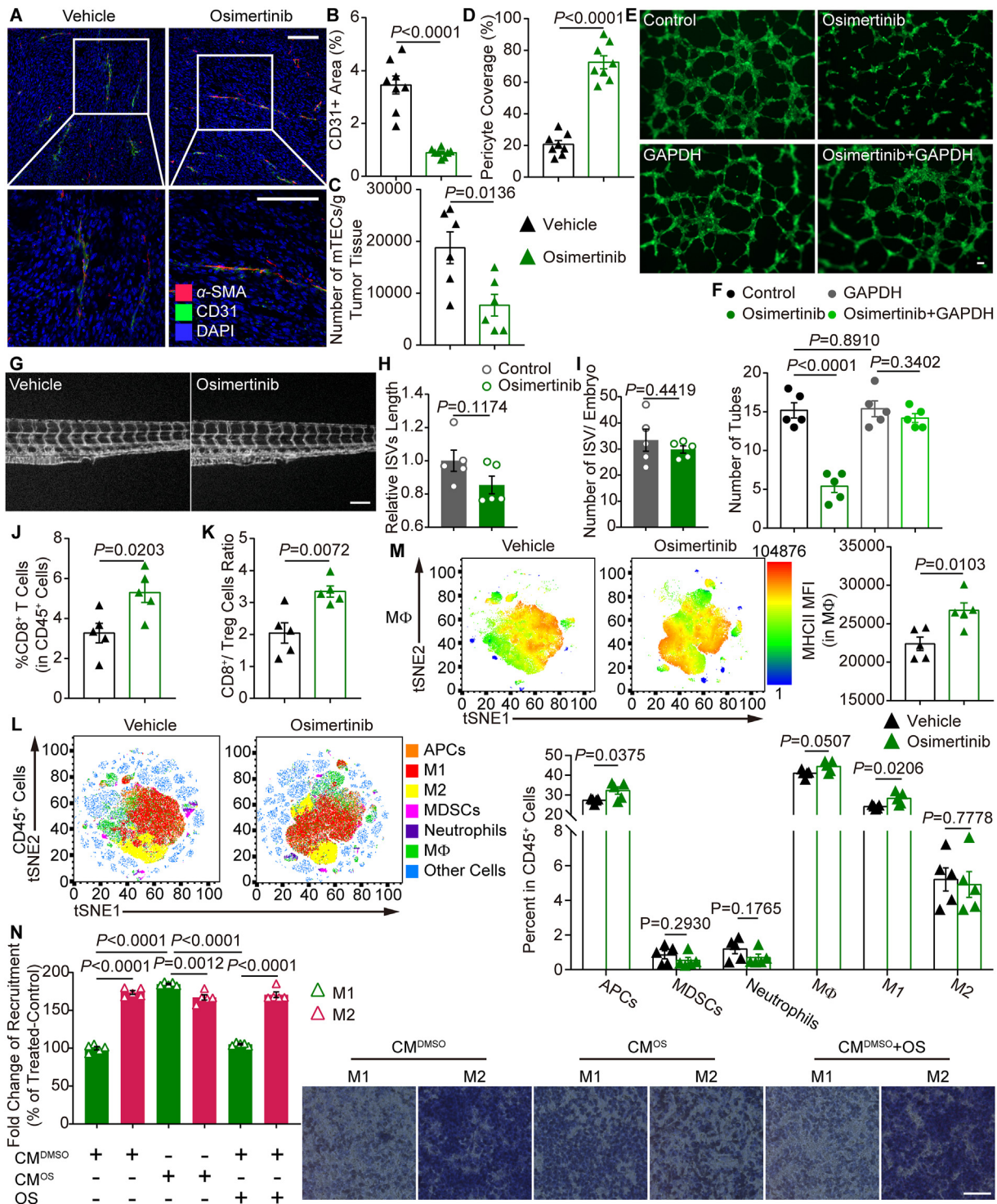
Figure 5 Osimertinib ameliorates tumor angiogenesis and triggers antitumor-macrophages infiltration. (A) Representative images of CD31 (green) and α-SMA (red) immunostaining, and DAPI nuclear staining (blue) of MC38 tumors treated with vehicle and osimertinib (1 mg/kg) daily for 14 days by oral gavage. (B) Relative CD31$^+$ area in tumors of two indicated groups. Each dot indicates one tumor per mouse and represents the average of 5 images. $n = 8$. (C) Total number of CD31$^+$ cells from tumor in vehicle group and osimertinib group determined by flow cytometry. $n = 6$. (D) Relative proportion of α-SMA$^+$ pericyte-covered blood vessels in tumors of two indicated groups. Each dot indicates one tumor and represents the average of 5 images. $n = 8$. (E) Representative images of endothelial tubular network in HUVECs treated with osimertinib (1 μmol/L) or DMSO for 24 h after overexpression with GAPDH vector for 24 h. (F) Quantification of tubes in experiments as in (E). (G) Representative photographs of the tail area of zebrafish embryos treated with osimertinib (1 μmol/L) or DMSO for 12 h. (H, I) Quantification of filopodia length (H) and number of ISV (I) in experiments as in G. (J) Quantification of CD8$^+$ T cells from MC38 tumors in vehicle group and osimertinib group. (K) Ratio of CD8$^+$ T cells to FOXP3$^+$CD25$^+$ regulatory T cells in MC38 tumors treated with vehicle or osimertinib. (L) Left,

process referred to as "vascular normalization"[3]. Apart from improving tumor oxygenation and drug penetration, vascular normalization facilitates the trafficking and functions of immune cells, including T cells, macrophages (MΦ), antigen-presenting cells (APCs) in tumor[29−31]. Thus, the effects of osimertinib on tumor immune microenvironment were further investigated. Various immune cell subsets in tumors were analyzed by flow cytometry (Supporting Information Fig. S6A and S6B). Osimertinib remarkably increased the percentage of CD8$^+$ T cells (Fig. 5J), as well as the CD8/Treg (Foxp3$^+$CD25$^+$) ratio (Fig. 5K) in tumors. We also found that osimertinib increased the absolute numbers of infiltration of CD8$^+$ T cells especially in the perivascular space of MC38 tumors (Fig. S6C). Both CD4$^+$ and CD8$^+$ T cells in tumors from osimertinib group produced more IFNγ compared to those from vehicle group (Fig. S6D and S6E). In addition, there were increased number of M1-like macrophages following the treatment of osimertinib, but no obvious changes in the local presence of APCs, myeloid-derived suppressor cells (MDSCs), neutrophils, M2-like macrophages and total MΦ (Fig. 5L). The combination of viSNE and heatmap analysis of flow cytometric data revealed a complex cellular landscape of MΦ with increased MHCII in osimertinib group compared with vehicle group (Fig. 5M). Next, the average mRNA level of *GAPDH* was used to estimate the cytotoxic T lymphocyte (CTL) infiltration level in CRC from the GEO database. It was found that high CTL level indicated improved overall survival of CRC patients, but only when *GAPDH* was at a low expression level (Fig. S6F and S6G). These observations suggest that osimertinib may induce T cell infiltration or recognition by antigen-presenting machinery of the macrophage population.

We next determined whether osimertinib could convert the immunosuppressive phenotype by repressing the glycolysis pathway and the end product lactate in TECs. The lactate levels were decreased in tumors treated with osimertinib (Supporting Information Fig. S7A). In addition, the levels of VEGF and TNFα (Fig. S7B and S7C) and the gene expression profiles (Fig. S7D) revealed that osimertinib controlled M1-like/M2-like macrophage recruitment or differentiation in tumors. To forge a direct link between the lactate level and macrophage recruitment, Boyden chambers were used to examine the migration of macrophages derived from peripheral blood mononuclear cells (PBMCs) of the same patient (Supporting Information Fig. S8A) by plating them into the inserts with conditioned medium from HUVECs in the lower wells. The transwell migration assay demonstrated that the conditioned medium from HUVECs increased the chemoattraction of M2-like macrophages compared with M1-like macrophages (Fig. 5N). Furthermore, the

conditioned medium from osimertinib-treated HUVECs restored the migration of M1-like macrophages. Interestingly, osimertinib was not able to directly chemoattract M1-like macrophages. Either GAPDH overexpression (Fig. S8B) or lactate treatment (Fig. S8C) abolished the effect of osimertinib on the increased M1-like macrophage migration, suggesting that osimertinib increased the recruitment of M1-like macrophages by inhibiting lactate secretion derived from ECs.

Altogether, these results indicate that osimertinib acts as a GAPDH mitigator that favors the tumor blood vessel pruning and antitumoral macrophages infiltration in CRC, independently of its mutant-EGFR inhibition.

3.6. The antitumoral activity of osimertinib is macrophage-dependent in the mouse CRC model

As mentioned above, osimertinib normalized the existing blood vessels and favorably improved the infiltration of immune cells. To solidify the role of osimertinib in the enhancement of immune response in CRC, MC38 tumor-bearing *Rag1*$^{−/−}$ mice were used. Osimertinib treatment in *Rag1*$^{−/−}$ mice partially delayed the tumor growth, but there were no significant differences in the tumor volume (Fig. 6A) or tumor weight (Fig. 6B) between vehicle group and osimertinib group. However, osimertinib still decreased the vascular density and increased α-SMA$^+$ pericyte coverage on tumor vessels in *Rag1*$^{−/−}$ mice (Fig. 6C−E). In addition, immunostaining showed that osimertinib had no significant effect on the proliferation and apoptosis of tumor cells compared with the vehicle group (Fig. 6F and G). To further verify whether CD8$^+$ CTLs were prerequisite effector cells responsible for the tumor inhibition by osimertinib, CD8$^+$ T cells were depleted by CD8-antibodies in MC38 tumor-bearing mice treated with osimertinib. Indeed, compared with vehicle group, osimertinib showed little inhibition of the tumor growth after CD8$^+$ T cells depletion (Fig. 6H). Furthermore, osimertinib did not provide substantial survival benefits in the above mouse model (Fig. 6I). These results suggest that antitumor effect of osimertinib is dependent on CD8$^+$ T cell response.

Given the therapeutic effect of osimertinib on driving the infiltration of M1-like macrophages, we proposed that macrophages induced the infiltration of CD8$^+$ T cells. To verify this hypothesis, macrophages were depleted *in vivo* using antibodies against CSF-1. Similar results were obtained that CSF-1 depletion strategy abrogated the efficacy of osimertinib on tumor growth (Fig. 6J) and survival (Fig. 6K) in the transplanted MC38 tumors. These data suggest that activated macrophages are indeed required for the antitumoral effect of osimertinib.

PhenoGraph of cellular distribution and clustering, as defined by tSNE1 and tSNE2, colored by cellular phenotype of MC38 tumors in vehicle group and osimertinib group. Data show all normalized viable single cells, subjected to the PhenoGraph algorithm. Right, quantification of tumor-infiltrating immune (CD45$^+$) cells in Vehicle group and osimertinib group, assessed by flow cytometry. Cell populations were identified as APCs (CD45$^+$CD11b$^+$CD11c$^+$MHCII$^+$), MΦ (CD45$^+$CD11b$^+$Gr-1$^-$F4/80$^+$), M1-like macrophages (CD45$^+$CD11b$^+$Gr-1$^-$F4/80$^+$CD11c$^+$CD206$^-$), M2-like macrophages (CD45$^+$CD11b$^+$Gr-1$^-$F4/80$^+$CD11c$^-$CD206$^+$), MDSCs (CD45$^+$CD11b$^+$Gr-1$^+$F4/80$^-$), and neutrophils (CD45$^+$CD11b$^+$CD11c$^-$Gr-1$^+$). (M) Left, viSNE analysis of immune cells from vehicle group and osimertinib group tumors colored by relative expression of MHCII in MΦ. Right, flow cytometry analysis of the major histocompatibility complex class II (MHCII) on MΦ from MC38 tumors. (N) HUVECs were treated with osimertinib (1 μmol/L) or DMSO in serum-free medium for 12 h. Left, statistical analyses of migrated LPS-activated M1-like or IL-4-activated M2-like macrophages attracted by conditioned medium (100 °C, 5 min) from either HUVEC-CM^{DMSO} or HUVEC-CM^{OS} and treated with osimertinib (1 μmol/L) or DMSO, additionally. Right, representative images of Transwell migration assays are shown. (E−N) $n = 5$. Statistical analysis by unpaired Student's *t*-test or one-way ANOVA. Data are presented as mean $\pm$ SEM. Scale bar = 100 μm.
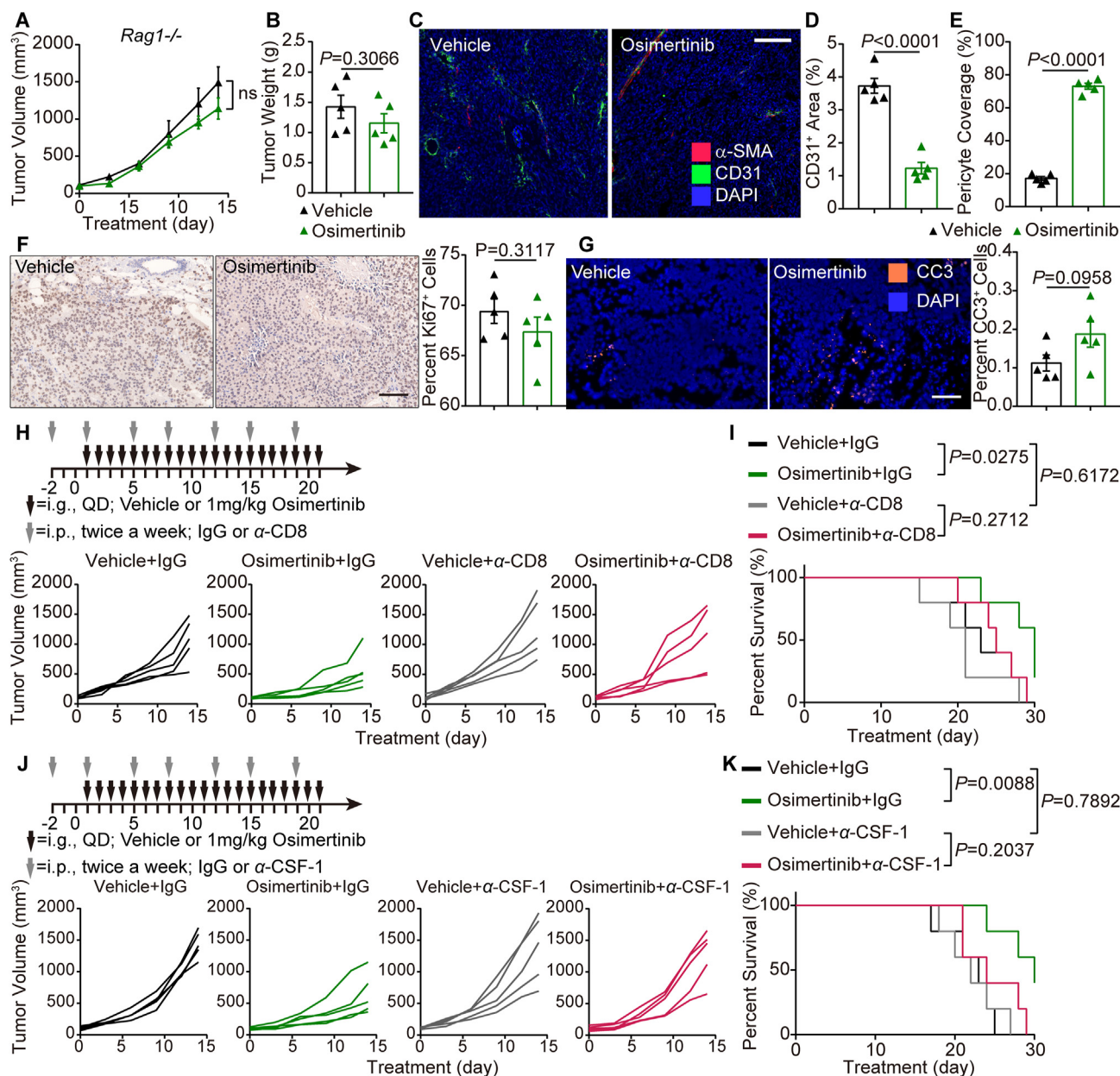
Figure 6 The antitumoral activity of osimertinib is macrophage-dependent in the mouse CRC model. (A) Volume of subcutaneous MC38 tumors form $Rag1^{-/-}$ mice in two indicated groups. $n = 6$. (B) Tumor weight at necropsy in two indicated groups treated as A. $n = 6$. (C) Representative images of CD31 (green) and α-SMA (red) immunostaining, and DAPI nuclear staining (blue) of tumors in vehicle group and osimertinib group. (D) Relative CD31$^+$ area in tumors of two indicated groups. Each dot indicates one tumor per mouse and represents the average of 5 images. (E) Relative proportion of α-SMA$^+$ pericyte-covered blood vessels in tumors of two indicated groups. Each dot indicates one tumor and represents the average of 5 images. (F) Left, representative images of Ki67 immunostaining (green) and nuclear staining (blue) of tumors in two indicated groups. Right, relative nuclear Ki67 in vehicle group and osimertinib group. Each dot indicates one tumor and represents the average of 5 images. (G) Left, representative images of cleaved caspase-3 (orange) and DAPI nuclear staining (blue) of tumors in two indicated groups. Right, relative cell death in vehicle group and osimertinib group. Each dot indicates one tumor per mouse and represents the average of 5 images. (H, J) Top, schematic of the workflow for treatment as indicated. Bottom, growth curves of individual tumors from indicated groups. (I, K) Kaplan−Meier survival curves of mice treated as indicated. (D−K) $n = 5$. Statistical analysis by unpaired Student's t-test or log-rank test. Data are presented as mean $\pm$ SEM. Scale bar = 100 μm.

3.7. Osimertinib and PD-1 blockade produces the synergistic effect on the antitumor activity in the CRC patient and mouse model

Tumor blood vessel imaging revealed a direct correlation between osimertinib and the expression of PD-L1 on TECs in the transplanted MC38 tumors (Fig. 7A). Furthermore, flow cytometry analysis showed that osimertinib raised the PD-L1 expression in CD45$^-$CD31$^+$ ECs of tumors (Fig. 7B).

Next, we investigated whether osimertinib could be an immune-enhancer for PD-1 antibody. Single treatment with anti-PD-1 (100 μg per body intraperitoneally) had no therapeutic effect (Fig. 7C). Notably, osimertinib potently synergized with anti-PD-1 therapy in reducing mouse tumor burden (Fig. 7C). The administration of anti-PD-1 and osimertinib significantly increased the survival compared with anti-PD-1 alone (Fig. 7D), indicating that the combination therapy could successfully elicit antitumor immunity. Additionally, we did not observe any body weight loss of mice in the combination treatment group (Supporting Information Fig. S9A). Collectively, these data demonstrated that osimertinib in combination with anti-PD-1 antibody potentiates the antitumor effect in the CRC mouse model.

Based on the therapeutic effect of osimertinib in combination with PD-1 antibody in mice, the possible efficacy and toxicity in CRC patients were further investigated. A 53-year-old patient underwent a radical resection of colon cancer, and the postoperative pathological stage was pT3N1M0 (IIIB). After four cycles of adjuvant chemotherapy with capecitabine and oxaliplatin, pulmonary metastases occurred in the patient. He then received multi-line treatments with irinotecan, 5-fluorouracil, raltitrexed, bevacizumab and regorafenib, but the metastatic foci were not effectively attenuated. Considering the negative PD-L1

expression, low tumor mutation burden (TMB) and microsatellite stability (MSS) phenotype in the tumor (Fig. S9B–S9D), the patient was treated with osimertinib plus sintilimab (PD-1 antibody). Surprisingly, the lung metastatic foci shrank significantly after four cycles without any obvious adverse reactions (Fig. S9E). On the basis of this case, we can speculate that osimertinib combined with PD-1 antibody might be a potential regimen for MSS CRC patients who relapse after multi-line therapy.

4. Discussion

The sprouting of new blood vessels executes an insidious ability to nourish expansive growth of cancer cells from nearby vessels of neighboring nonmalignant tissues in solid tumors[32]. Endothelial hyperglycolysis is an important metabolic signature that meets the needs of rapid proliferation and increased motility in cancer, and dictates the drug target to the treatment[33,34]. Previous studies have focused on eradicating glycolysis in ECs[35,36], while normalizing hyperglycolysis back to basal condition has remained an uncharted territory. ECs could reprogram metabolic adaptations, including fatty acid metabolism, serine metabolism, glutamine and asparagine metabolism, for angiogenesis after glycolysis blockade[19]. Thus, it is important to study the normalization of endothelial metabolism in solid tumors.

In the present study, we confirmed that endothelial glycolysis was relatively high in the tumor stromal compartment compared with glycolysis in the adjacent tissue compartment in the clinical CRC patients and mouse models. GAPDH is a key stimulator of the metabolic switch in the glycolytic pathway, which is profoundly needed only in wildly proliferating cells[37]. Through screening FDA-approved kinase and non-kinase inhibitors, we identified a glycolytic mitigator osimertinib that inactivated GAPDH by modifying the
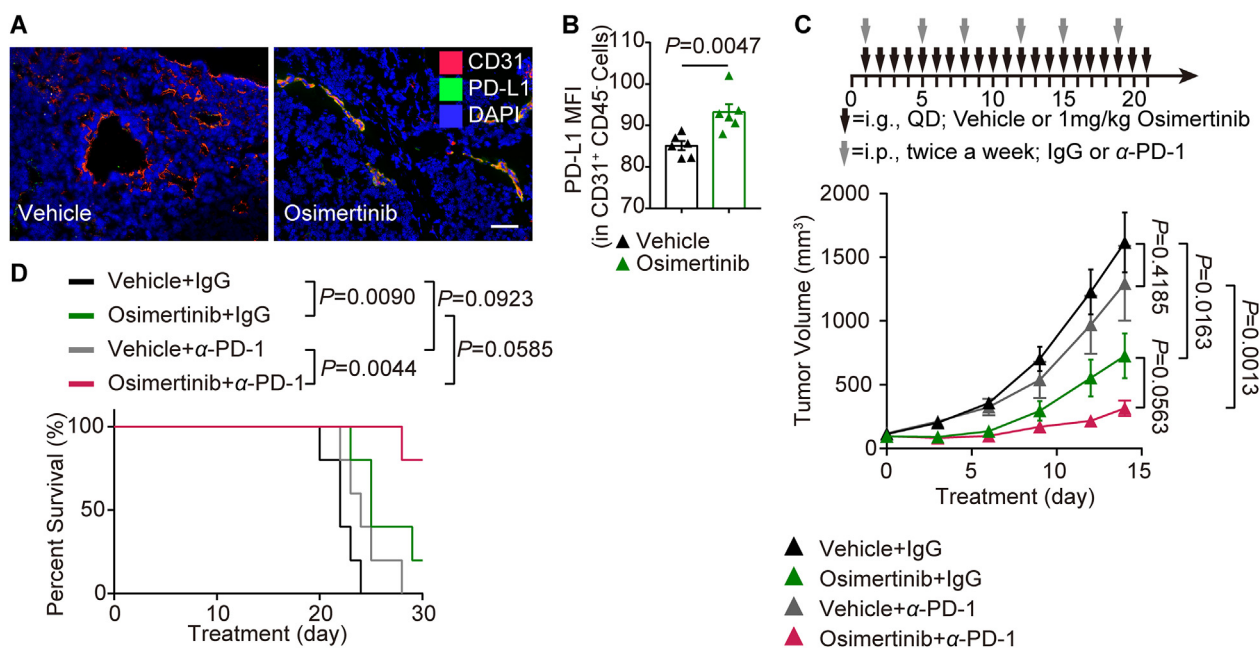
Figure 7 Osimertinib and PD-1 blockade produces the synergistic effect on the antitumor activity in the CRC patient and mouse model. (A) Representative images of CD31 (red) and PD-L1 (green) immunostaining and DAPI nuclear staining (blue) of tumors in vehicle group and osimertinib group. (B) Flow cytometry analysis of PD-L1 expression in CD45$^-$CD31$^+$ endothelial cells of tumors in two indicated groups. $n = 6$. (C) Top, schematic of the workflow for treatment as indicated. Bottom, growth of individual tumors from indicated groups. (D) Kaplan–Meier survival curves of mice treated as indicated. (C, D) $n = 5$. Statistical analysis by unpaired Student's t-test, one-way ANOVA or log-rank test. Data are presented as mean ± SEM. Scale bar = 100 μm.

residue Cys247. In line with our study, Samson and colleagues[38] provided the evidence that GAPDH diminished glycolytic activity, when it possessed cysteine-free variant (C152S, C156S, and C247S).

Up to now, there are 62 protein kinase inhibitors and a lot of small molecule non-kinase inhibitors approved by the FDA[39]. However, major acquired resistance has been observed after several months of treatment[40]. We intended to explore new therapeutic effects of FDA-approved drugs. Osimertinib, a third generation of EGFR-TKI, is an irreversible orally available indole-pyrimidine derivative[41]. It has been approved for treatment of advanced or metastatic non-small cell lung cancer (NSCLC) patients with EGFR L858R mutation or T790M mutation in clinic[42]. Moreover, osimertinib has shown favorable efficacy over erlotinib or gefitinib in EGFR-positive NSCLC patients with brain metastases[43]. Nevertheless, acquired resistance to osimertinib occurs in almost all patients after 10−12 months of treatment[44]. In addition, there are not many patients with NSCLC treated with osimertinib, because only EGFR T790M mutates after TKI resistance in NSCLC patients[45]. Our data identified a novel combination strategy to extend the tolerability of osimertinib.

Metabolic normalization is receiving increasing attention as an alternative therapeutic strategy[19]. Compared with the glycolytic inhibitors 3PO or Compound 3K, which completely eliminate glycolysis in all proliferating TECs[36,46], osimertinib works as a specific mitigator of endothelial glycolysis in anti-angiogenesis, without affecting normalized glycolysis. Under the treatment with very-low-dose osimertinib (1 mg/kg), TECs acquired maturation and quiescence. Our ECAR assay showed that osimertinib substantially normalized the glycolysis level in mTECs, which was consistent with that of mNECs in the preclinical study. It was conceivable that ECs integrated into the vessel wall and stimulated pericyte coverage by osimertinib. However, most previous preclinical and clinical studies tended to use high-dose osimertinib for directly killing tumor cells[47,48], but they switched the endothelial metabolism. This provides another rationale for osimertinib resistance. Meanwhile, our data explained the results of Akamatsu's study[49], which showed that the combination of osimertinib with bevacizumab failed to prolong the progression free survival (PFS) in patients compared with osimertinib monotherapy, by proving the new role of osimertinib in anti-angiogenesis.

This discovery that osimertinib emerges as a potential glycolytic normalized drug might allow the design of better combinational treatments, including therapy of immunometabolism. We hypothesized that osimertinib could trigger overall antitumor immunity response. Indeed, we found that osimertinib facilitated the activated CD8+ CTL trafficking and subsequently increased the CD8/Treg ratio. In addition, osimertinib induced M1-like macrophage infiltration and extensive tumor necrosis in mouse CRC models, which enhanced the cross-priming capacity for tumor-specific T cell activation. The above results supported the notion that normalization of tumor blood vessels not only allowed for T cell extravasation, but also recruited innate immune cells, thereby promoting the deployment of antitumor immunity[50,51].

Next, we demonstrated that the antitumor efficacy of osimertinib disappeared in $Rag1^{-/-}$ mouse, which cannot generate mature T and B cells, while the inhibition of angiogenesis by osimertinib still existed. Besides, depletion of CD8+ T cells or macrophages by neutralizing antibodies abrogated the efficacy of osimertinib in the mouse CRC models. These observations suggested that macrophages might mediate crucial antitumor responses induced by osimertinib in the context of antiangiogenic therapy. Our study enhanced the current understanding of antiangiogenic therapy combined with immunotherapy[6]. Another intriguing finding was the increased M1-like macrophage recruitment by osimertinib. These data could be explained by reduced lactate secretion due to osimertinib treatment through normalizing glycolysis in TECs. Although previous observations shown that lactate delivery resulted in M2-like macrophages polarization[13], our data revealed that endothelial lactate inhibited M1-like macrophage infiltration into the tumor microenvironment.

Accumulating studies showed that lactate was critical for facilitating tumor cell immune escape through maintaining
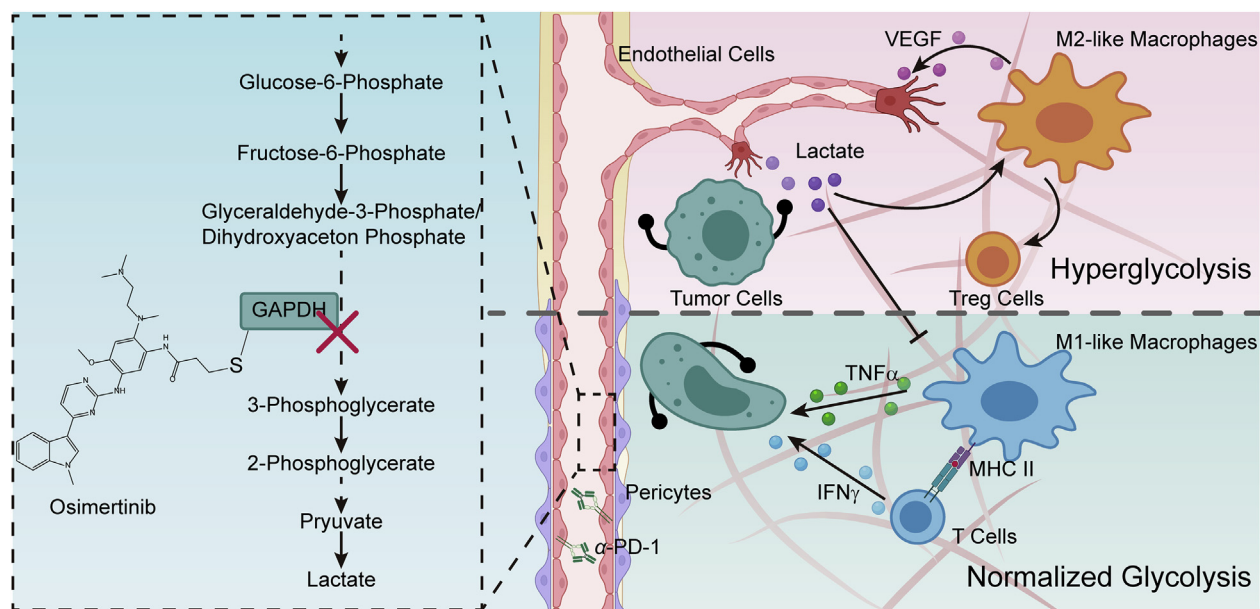
Figure 8 Diagram depicting the changes in tumor microenvironment triggered by endothelial GAPDH inactivation *via* osimertinib modification in CRC. Figure created with BioRender (https://biorender.com).

immunosuppressive function of Tregs and tumor-associated macrophages[52−54]. However, whether ECs or tumor autonomous lactate is more essential depends on the different caner type[33]. Here, we showed that osimertinib exhibited a high distribution in tumor, predominantly in TECs compared with other cells in the tumor tissues of the mouse CRC model. Thus, we inferred that the reduction of lactate in tumors apparently relied on TECs.

In the osimertinib monotherapy experiments, we observed that very-low-dose osimertinib (1 mg/kg) markedly extended the survival and delayed tumor growth, whereas upregulation of endothelial PD-L1 induced by IFNγ from activated T cells caused a limited antitumor immune effect[55]. In our preclinical part of the study, we uncovered that osimertinib in combination with PD-1 antibody had synergistic antitumor activity. Notably, our clinical results further supported the hypothesis. Namely, lung metastatic foci of a CRC patient disappeared rapidly after the combination treatment with osimertinib and sintilimab. Although clinical data was intriguing, we have also noticed a large number of studies have found that the combination of TKI and anti-PD-L1 were terminated due to a 40% pneumonitis rate in lung cancer[56]. According to EGFR mutations affect the tumor microenvironment in NSCLC, EGFR mutation may be one of the causes for severe pneumonia following the combination of TKI and anti-PD-L1[57]. So we emphasize that the preliminary human study requires larger sample sets and prospective analyses.

5. Conclusions

Our findings demonstrated that TECs exploited higher glycolytic characteristics to establish immunometabolic microenvironment for suppressing immune surveillance. Osimertinib-induced alkylation of the residue Cys247 of GAPDH in TECs functionally normalized hyperglycolysis back to baseline level, and subsequently reduced lactate secretion. Osimertinib can be effective in boosting anti-angiogenesis effects, as well as subsequent responses to metabolic immunotherapy. This study provides a potential strategy to enhance immunotherapy by targeting the abnormal metabolism of TECs (Fig. 8).

Acknowledgments

Author contributions

Yunlong Shan, Fang Zhou and Guangji Wang designed the project. Yunlong Shan conducted most experiments. Mengying Zhang, Qi Ni and Qixiang Zhang conducted some experiments related to mice and cell culture. Lingge Cheng and Chongjin Zhong performed IF and flow cytometer. Bin Wei and Jingjing Wu planned and conducted clinical study and analyzed the data. Qingqing Wang performed LC−MS/MS analysis. Xinyu Wang conducted ECAR monitor. Yunlong Shan wrote the preliminary paper. Fang Zhou and Guangji Wang revised and rewrote the paper. Jingwei Zhang and Jiali Liu provided help for manuscript discussion.

Conflicts of interests

The authors declare no conflict of interests.

Appendix A.   Supporting information

Supporting data to this article can be found online at https://doi.org/10.1016/j.apsb.2022.02.014.

References

1. Fridman WH, Miller I, Sautès-Fridman C, Byrne AT. Therapeutic targeting of the colorectal tumor stroma. *Gastroenterology* 2020;**158**:303−21.
2. Shaked Y. The pro-tumorigenic host response to cancer therapies. *Nat Rev Cancer* 2019;**19**:667−85.
3. De Palma M, Biziato D, Petrova TV. Microenvironmental regulation of tumour angiogenesis. *Nat Rev Cancer* 2017;**17**:457−74.
4. Apte RS, Chen DS, Ferrara N. VEGF in signaling and disease: beyond discovery and development. *Cell* 2019;**176**:1248−64.
5. Chaudhary A, Hilton MB, Seaman S, Haines DC, Stevenson S, Lemotte PK, et al. TEM8/ANTXR1 blockade inhibits pathological angiogenesis and potentiates tumoricidal responses against multiple cancer types. *Cancer Cell* 2012;**21**:212−26.
6. Yi M, Jiao D, Qin S, Chu Q, Wu K, Li A. Synergistic effect of immune checkpoint blockade and anti-angiogenesis in cancer treatment. *Mol Cancer* 2019;**18**:60.
7. Cheng L, Liu W, Zhong C, Ni P, Ni S, Wang Q, et al. Remodeling the homeostasis of pro- and anti-angiogenic factors by Shenmai injection to normalize tumor vasculature for enhanced cancer chemotherapy. *J Ethnopharmacol* 2020;**270**:113770.
8. Zhong C, Jiang C, Ni S, Wang Q, Cheng L, Wang H, et al. Identification of bioactive anti-angiogenic components targeting tumor endothelial cells in Shenmai injection using multidimensional pharmacokinetics. *Acta Pharm Sin B* 2020;**10**:1694−708.
9. Allen E, Jabouille A, Rivera LB, Lodewijckx I, Missiaen R, Steri V, et al. Combined antiangiogenic and anti-PD-L1 therapy stimulates tumor immunity through HEV formation. *Sci Transl Med* 2017;**9**:eaak9679.
10. Huang Y, Kim B, Chan CK, Hahn SM, Weissman IL, Jiang W. Improving immune−vascular crosstalk for cancer immunotherapy. *Nat Rev Immunol* 2018;**18**:195−203.
11. Meder L, Schuldt P, Thelen M, Schmitt A, Dietlein F, Klein S, et al. Combined VEGF and PD-L1 blockade displays synergistic treatment effects in an autochthonous mouse model of small cell lung cancer. *Cancer Res* 2018;**78**:4270−81.
12. Hegde PS, Chen DS. Top 10 challenges in cancer immunotherapy. *Immunity* 2020;**52**:17−35.
13. Zhang J, Muri J, Fitzgerald G, Gorski T, Gianni-Barrera R, Masschelein E, et al. Endothelial lactate controls muscle regeneration from ischemia by inducing M2-like macrophage polarization. *Cell Metabol* 2020;**31**:1136−53.
14. Yang Q, Xu J, Ma Q, Liu Z, Sudhahar V, Cao Y, et al. PRKAA1/AMPKα1-driven glycolysis in endothelial cells exposed to disturbed flow protects against atherosclerosis. *Nat Commun* 2018;**9**:4667.
15. Potente M, Carmeliet P. The link between angiogenesis and endothelial metabolism. *Annu Rev Physiol* 2017;**79**:43−66.

16. Fitzgerald G, Soro-Arnaiz I, De Bock K. The warburg effect in endothelial cells and its potential as an anti-angiogenic target in cancer. *Front Cell Dev Biol* 2018;**6**:100.

17. Eelen G, de Zeeuw P, Treps L, Harjes U, Wong BW, Carmeliet P. Endothelial cell metabolism. *Physiol Rev* 2018;**98**:3−58.

18. Jakobsson L, Franco CA, Bentley K, Collins RT, Ponsioen B, Aspalter IM, et al. Endothelial cells dynamically compete for the tip cell position during angiogenic sprouting. *Nat Cell Biol* 2010;**12**: 943−53.

19. Falkenberg KD, Rohlenova K, Luo Y, Carmeliet P. The metabolic engine of endothelial cells. *Nat Metab* 2019;**1**:937−46.

20. Wu D, Huang RT, Hamanaka RB, Krause M, Oh MJ, Kuo CH, et al. HIF-1α is required for disturbed flow-induced metabolic reprogramming in human and porcine vascular endothelium. *Elife* 2017;**6**: e25217.

21. Feng S, Bowden N, Fragiadaki M, Souilhol C, Hsiao S, Mahmoud M, et al. Mechanical activation of hypoxia-inducible factor 1α drives endothelial dysfunction at atheroprone sites. *Arterioscler Thromb Vasc Biol* 2017;**37**:2087−101.

22. Shevchenko A, Tomas H, Havlis J, Olsen JV, Mann M. In-gel digestion for mass spectrometric characterization of proteins and proteomes. *Nat Protoc* 2006;**1**:2856−60.

23. Chi H, Liu C, Yang H, Zeng WF, Wu L, Zhou WJ, et al. Comprehensive identification of peptides in tandem mass spectra using an efficient open search engine. *Nat Biotechnol* 2018;**36**:1059−61.

24. Chang CH, Curtis JD, Maggi Jr LB, Faubert B, Villarino AV, O'Sullivan D, et al. Posttranscriptional control of T cell effector function by aerobic glycolysis. *Cell* 2013;**153**:1239−51.

25. Kornberg MD, Bhargava P, Kim PM, Putluri V, Snowman AM, Putluri N, et al. Dimethyl fumarate targets GAPDH and aerobic glycolysis to modulate immunity. *Science* 2018;**360**:449−53.

26. Lomenick B, Hao R, Jonai N, Chin RM, Aghajan M, Warburton S, et al. Target identification using drug affinity responsive target stability (DARTS). *Proc Natl Acad Sci U S A* 2009;**106**:21984−9.

27. Nagasaka M, Zhu VW, Lim SM, Greco M, Wu F, Ignatius Ou SH. Beyond osimertinib: the development of 3rd-generation EGFR tyrosine kinase inhibitors. *J Thorac Oncol* 2021;**16**:5740−63.

28. Ballard P, Yates JW, Yang Z, Kim DW, Yang JC, Cantarini M, et al. Preclinical comparison of osimertinib with other EGFR-TKIs in EGFR-mutant NSCLC brain metastases models, and early evidence of clinical brain metastases Activity. *Clin Cancer Res* 2016;**22**:5130−40.

29. Fukumura D, Kloepper J, Amoozgar Z, Duda DG, Jain RK. Enhancing cancer immunotherapy using antiangiogenics: opportunities and challenges. *Nat Rev Clin Oncol* 2018;**15**:325−40.

30. Pavlova NN, Thompson CB. The emerging hallmarks of cancer metabolism. *Cell Metabol* 2016;**23**:27−47.

31. Galon J, Bruni D. Tumor immunology and tumor evolution: intertwined histories. *Immunity* 2020;**52**:55−81.

32. Kerbel RS. Tumor angiogenesis. *N Engl J Med* 2008;**358**:2039−49.

33. De Bock K, Georgiadou M, Schoors S, Kuchnio A, Wong BW, Cantelmo AR, et al. Role of PFKFB3-driven glycolysis in vessel sprouting. *Cell* 2013;**154**:651−63.

34. Yu P, Wilhelm K, Dubrac A, Tung JK, Alves TC, Fang JS, et al. FGF-dependent metabolic control of vascular development. *Nature* 2017; **545**:224−8.

35. Carmeliet P, Jain RK. Molecular mechanisms and clinical applications of angiogenesis. *Nature* 2011;**473**:298−307.

36. Cantelmo AR, Conradi LC, Brajic A, Goveia J, Kalucka J, Pircher A, et al. Inhibition of the glycolytic activator PFKFB3 in endothelium induces tumor vessel normalization, impairs metastasis, and improves chemotherapy. *Cancer Cell* 2016;**30**:968−85.

37. Shestov AA, Liu X, Ser Z, Cluntun AA, Hung YP, Huang L, et al. Quantitative determinants of aerobic glycolysis identify flux through the enzyme GAPDH as a limiting step. *Elife* 2014;**3**:e03342.

38. Samson AL, Knaupp AS, Kass I, Kleifeld O, Marijanovic EM, Hughes VA, et al. Oxidation of an exposed methionine instigates the

39. aggregation of glyceraldehyde-3-phosphate dehydrogenase. *J Biol Chem* 2014;**289**:26922−36.

39. Roskoski Jr R. Orally effective FDA-approved protein kinase targeted covalent inhibitors (TCIs). *Pharmacol Res* 2021;**165**:105422.

40. Vasan N, Baselga J, Hyman DM. A view on drug resistance in cancer. *Nature* 2019;**575**:299−309.

41. Finlay MR, Anderton M, Ashton S, Ballard P, Bethel PA, Box MR, et al. Discovery of a potent and selective EGFR inhibitor (AZD9291) of both sensitizing and T790M resistance mutations that spares the wild type form of the receptor. *J Med Chem* 2014;**57**:8249−67.

42. Yver A. Osimertinib (AZD9291)-a science-driven, collaborative approach to rapid drug design and development. *Ann Oncol* 2016;**27**: 1165−70.

43. Hochmair M. Medical treatment options for patients with epidermal growth factor receptor mutation-positive non-small cell lung cancer suffering from brain metastases and/or leptomeningeal disease. *Targeted Oncol* 2018;**13**:269−85.

44. Mok TS, Wu YL, Ahn MJ, Garassino MC, Kim HR, Ramalingam SS, et al. Osimertinib or platinum-pemetrexed in EGFR T790M-positive lung cancer. *N Engl J Med* 2017;**376**:629−40.

45. Zhu VW, Klempner SJ, Ou SI. Receptor tyrosine kinase fusions as an actionable resistance mechanism to EGFR TKIs in EGFR-mutant non-small-cell lung cancer. *Trends Cancer* 2019;**5**:677−92.

46. Stone OA, El-Brolosy M, Wilhelm K, Liu X, Romão AM, Grillo E, et al. Loss of pyruvate kinase M2 limits growth and triggers innate immune signaling in endothelial cells. *Nat Commun* 2018;**9**:4077.

47. Wu S, Luo M, To K, Zhang J, Su C, Zhang H, et al. Intercellular transfer of exosomal wild type EGFR triggers osimertinib resistance in non-small cell lung cancer. *Mol Cancer* 2021;**20**:17.

48. Yu HA, Paz-Ares LG, Yang JC, Lee KH, Garrido P, Park K, et al. Phase I study of the efficacy and safety of ramucirumab in combination with osimertinib in advanced T790M-positive EGFR-mutant non-small cell lung cancer. *Clin Cancer Res* 2020;**27**:992−1002.

49. Akamatsu H, Toi Y, Hayashi H, Fujimoto D, Tachihara M, Furuya N, et al. Efficacy of osimertinib plus bevacizumab *vs* osimertinib in patients with EGFR T790M-mutated non-small cell lung cancer previously treated with epidermal growth factor receptor-tyrosine kinase inhibitor: west Japan oncology group 8715L phase 2 randomized clinical trial. *JAMA Oncol* 2021;**7**:386−94.

50. Schmittnaegel M, Rigamonti N, Kadioglu E, Cassará A, Wyser Rmili C, Kiialainen A, et al. Dual angiopoietin-2 and VEGFA inhibition elicits antitumor immunity that is enhanced by PD-1 checkpoint blockade. *Sci Transl Med* 2017;**9**:eaak9670.

51. Park JS, Kim IK, Han S, Park I, Kim C, Bae J, et al. Normalization of tumor vessels by Tie2 activation and Ang2 inhibition enhances drug delivery and produces a favorable tumor microenvironment. *Cancer Cell* 2016;**30**:953−67.

52. Angelin A, Gil-de-Gómez L, Dahiya S, Jiao J, Guo L, Levine MH, et al. Foxp3 reprograms T cell metabolism to function in low-glucose, high-lactate environments. *Cell Metabol* 2017;**25**:1282−93.

53. Liu N, Luo J, Kuang D, Xu S, Duan Y, Xia Y, et al. Lactate inhibits ATP6V0d2 expression in tumor-associated macrophages to promote HIF-2α-mediated tumor progression. *J Clin Invest* 2019;**129**:631−46.

54. García-Cañaveras JC, Chen L, Rabinowitz JD. The tumor metabolic microenvironment: lessons from lactate. *Cancer Res* 2019;**79**:3155−62.

55. Peng W, Liu C, Xu C, Lou Y, Chen J, Yang Y, et al. PD-1 blockade enhances T-cell migration to tumors by elevating IFN-γ inducible chemokines. *Cancer Res* 2012;**72**:5209−18.

56. Oxnard GR, Yang JC, Yu H, Kim SW, Saka H, Horn L, et al. TATTON: a multi-arm, phase Ib trial of osimertinib combined with selumetinib, savolitinib, or durvalumab in EGFR-mutant lung cancer. *Ann Oncol* 2020;**31**:507−16.

57. Lin A, Wei T, Meng H, Luo P, Zhang J. Role of the dynamic tumor microenvironment in controversies regarding immune checkpoint inhibitors for the treatment of non-small cell lung cancer (NSCLC) with EGFR mutations. *Mol Cancer* 2019;**18**:139.